Diamond & Related Materials 155 (2025) 112247

Contents lists available at ScienceDirect

Diamond & Related Materials

journal homepage: www.elsevier.com/locate/diamond

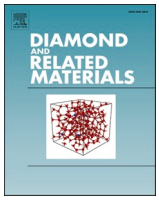

# Holey graphene films intercalated with iron nanoparticles for efficient electromagnetic wave shielding

Xingnian Li [a], Fei Wang [b], Qiang Li [a,*], Chuanren Ye [b,*], Yingyu Chen [a], Jingwei Li [a], Hui Lin [a], Jingwei Zhang [c], Yanwu Zhu [b,d,**]

[a] School of Physics, Hefei University of Technology, Hefei, Anhui 230009, China
[b] Department of Materials Science and Engineering, School of Chemistry and Materials Sciences, University of Science and Technology of China, Hefei, Anhui 230026, China
[c] National and Local Joint Engineering Research Center for Applied Technology of Hybrid Nanomaterials, Henan University, Kaifeng 475004, China
[d] Hefei National Research Center for Physical Sciences at the Microscale & CAS Key Laboratory of Materials for Energy Conversion, University of Science and Technology of China, Hefei, Anhui 230026, China

ARTICLE INFO

*Keywords:*
Graphene
Electromagnetic interference shielding
Iron nanoparticles
Microholes

ABSTRACT

With excellent electrical conductivity and engineering feasibility, graphene materials have attracted increasing attention in the application of electromagnetic interference (EMI) shielding, where graphene-based composites are considered to achieve a better EMI shielding effectiveness (EMI SE) than the bare graphene films. In this study, holey graphene films intercalated with iron nanoparticles (FRGO) are fabricated through a two-step filtration and thermal annealing method, in which the initially intercalated $BiFeO_3$ microparticles are thermally decomposed to iron nanoparticles and create microholes in graphene simultaneously. Due to multiple reflections within microholes and the magnetic loss generated by the iron nanoparticles in response to electromagnetic waves, the FRGO-6:40 film (where 6:40 represents the mass ratio of $BiFeO_3$ to graphene oxide in the precursor mixture) with a thickness of 71 μm reaches an excellent EMI SE of 38.64 dB at 9.9 GHz within the X-band range (8.2–12.5 GHz). We find that although the electrical conductivity of the holey graphene film decreases when intercalated by iron nanoparticles, the EMI SE increases, attributed to the enhancement in electromagnetic wave absorption contributed by iron nanoparticles and microholes.

## 1. Introduction

The explosive growth in the use of electronic devices and wireless communication has significantly exacerbated the perils of electromagnetic interference (EMI), which has sparked intense concerns regarding information security, signal interception and human health. [1–6] Traditionally, metallic materials are used to control undesirable electromagnetic radiation, but are restricted in practical applications due to their high density, corrosiveness and strong secondary electromagnetic waves. [7,8] Despite of the significant advancement of 2D MXene, [9] research of lightweight and chemically stable carbon materials with superior electrical conductivity for specialized application of EMI shielding becomes attractive in recent years. [10,11] Among carbon materials, graphene has attracted intensive attentions by the great feasibility of solution-processing into assemblies such as films [12,13], aerogels [14] and fibers [15] with controllable structure and composite, making it an ideal EMI shielding material. [16,17] In graphene-based materials, the dielectric loss, which includes conduction loss and polarization loss, dominates the electromagnetic wave attenuation. [18] Therefore, addressing the issues of single loss mechanism has been an ongoing research for the EMI application of graphene materials.

Introducing magnetic loss into graphene materials convents electromagnetic energy into thermal energy by the eddy current effect and magnetic resonance to improve the EMI shielding performance of graphene magnetic composites. [19,20] Qiu et al. prepared magnetic graphene oxide (MGO) by loading $Fe_3O_4$ nanoparticles onto graphene oxide (GO), and the EMI SE of the carbon fiber wrapped with MGO reached 46.33 dB in the X-band, which is 8.42 dB higher than that of the original

* Corresponding authors.
** Correspondence to: Y.W. Zhu, Hefei National Research Center for Physical Sciences at the Microscale & CAS Key Laboratory of Materials for Energy Conversion, University of Science and Technology of China, Hefei, Anhui 230026, China.
*E-mail addresses:* qli@hfut.edu.cn (Q. Li), ycr19@ustc.edu.cn (C. Ye), zhuyanwu@ustc.edu.cn (Y. Zhu).

https://doi.org/10.1016/j.diamond.2025.112247
Received 25 January 2025; Received in revised form 10 March 2025; Accepted 25 March 2025
Available online 28 March 2025

carbon fiber. [21] Moreover, constructing pores in graphene or its composites would induce extra multiple reflections of electromagnetic wave in the internal pores, [22] thereby enhancing the absorption ability to electromagnetic wave. [23,24] Kashani et al. prepared graphene membrane with bi-continuous nanoporosity by using nanoporous nickel as sacrificial template through chemical vapor deposition (CVD) method, which exhibites an EMI SE of 59 dB with a thickness of 150 μm. [25] Therefore, synergistic effects of multiple electromagnetic loss mechanism and porous structure can be achieved by properly designing the graphene composites. The EMI SE of flexible three-dimensional (3D) porous graphene films combined with nickel nanoparticles reached 79 dB for thickness of 327 μm. [26] Besides nickel nanoparticles, iron nanoparticles were also able to enhance the electromagnetic wave absorption of the carbon-based materials but the coupling between iron loss and structural loss remains to be investigated. [27]

Herein, a facile and controllable preparation of holey graphene films intercalated with iron nanoparticles is reported. A two-step filtration and annealing process is used to intercalate $BiFeO_3$ particles into graphene oxide film (FGO) and reduce the FGO film at 1000 °C in a nitrogen atmosphere, during which $BiFeO_3$ particles are decomposed into iron nanoparticles and microholes are simultaneously created in the reduced GO, resulting in samples named as FRGO. When the appropriate amount of $BiFeO_3$ particles is introduced, the EMI SE performance is improved due to the combined benefit from multiple reflections of electromagnetic waves by the microholes and the magnetic loss induced by the iron nanoparticles, although the electrical conductivity of FRGO films is lower than that of rGO film. The optimized film (FRGO-6:40) with a thickness of 71 μm reaches an excellent EMI SE of 38.64 dB at 9.9 GHz.

## 2. Experiments

### 2.1. Chemicals and materials

$Fe(NO_3)_3{\cdot}9H_2O$, $Bi(NO_3)_3{\cdot}5H_2O$ and NaOH were obtained from Aladdin Industrial Co., Ltd. $C_2H_6O_2$ was purchased from Shanghai Macklin Biochemical Technology Co., Ltd. $NH_3{\cdot}H_2O$ was obtained from Sinopharm Chemical Reagent Co., Ltd. Polyvinylidene fluoride (PVDF) membrane with a pore size of 0.44 μm was purchased from Tianjin Jinteng Technology Co., Ltd. Graphite oxide was obtained from The Sixth Element (Changzhou) Materials Technology Co., Ltd.

### 2.2. Preparation of $BiFeO_3$ particles

5 mmol $Bi(NO_3)_3{\cdot}5H_2O$ and 5 mmol $Fe(NO_3)_3{\cdot}9H_2O$ were dissolved in 15 ml Glycol ($C_2H_6O_2$) and stirred for 5 min at 50 °C. Then, 100 ml deionized water was added into the solution. After stirring for 5 min, 8 ml $NH_3{\cdot}H_2O$ was introduced and stirred for 20 min. The obtained mixture was centrifugated at 5000 rpm for 5 min and the sediment was collected and washed by deionized water twice. The separated precursor was then mixed with 30 ml 0.15 M NaOH solution and heated at 180 °C for 16 h in a 50 ml hydrothermal vessel. Subsequently, a centrifugation at 6000 rpm was conducted to remove the supernatant. After washing with deionized water twice, the collected sediment of $BiFeO_3$ powder was dried at 80 °C for 4 h in vacuum and slightly grinded.

### 2.3. Preparation of FRGO film

Commercial graphite oxide was dispersed in deionized water with a concentration of 2 mg $ml^{-1}$ by stirring at 450 rpm for 2 h to prepare GO solution. The FRGO film was prepared by vacuum filtration and thermal treatment, as shown in Fig. 1. Firstly, 10 ml GO dispersion (2 mg $mL^{-1}$) was adopted for preparing underlying film by vacuum filtration (vacuum filtration-I). Before the assembled GO film was completely dried, another 10 ml GO dispersion mixed with a certain amount of $BiFeO_3$ was introduced to prepare the upper layer film (vacuum filtration-II). According to the mass of $BiFeO_3$ added, the GO/$BiFeO_3$ composite film is named as FGO-2:40, FGO-6:40, FGO-10:40, FGO-15:40, and FGO-20:40, where, for example, FGO-6:40 consists of 6 mg $BiFeO_3$ and 40 mg GO. As a control sample, a bare GO film was prepared by vacuum filtration of 20 ml GO dispersion (40 mg). Then, the heat treatment of GO and FGO film was conducted at 1000 °C for 2 h in a nitrogen atmosphere (100 sccm). The obtained films from GO and FGO are labeled as rGO and FRGO. For example, FRGO-6:40 was prepared from FGO-6:40.

### 2.4. Characterizations

Scanning electron microscopy (SEM; Gemimi 500, Carl Zeiss, Germany) was employed to characterize the morphology and particle distribution of the composite films. Raman spectroscopy (LabRAM HR Evolution) was performed with an excitation wavelength of 785 nm. X-ray diffraction (XRD, PANalytical X-PERT PRO MPD) was performed on the films at a diffraction angle from 5° to 70° with a source of Cu $K_{\alpha1}$ radiation ($\lambda = 0.15405$ nm). A multifunctional digital four-probe tester (ST-2258C; Suzhou Jingge) was used for the measurement of electrical

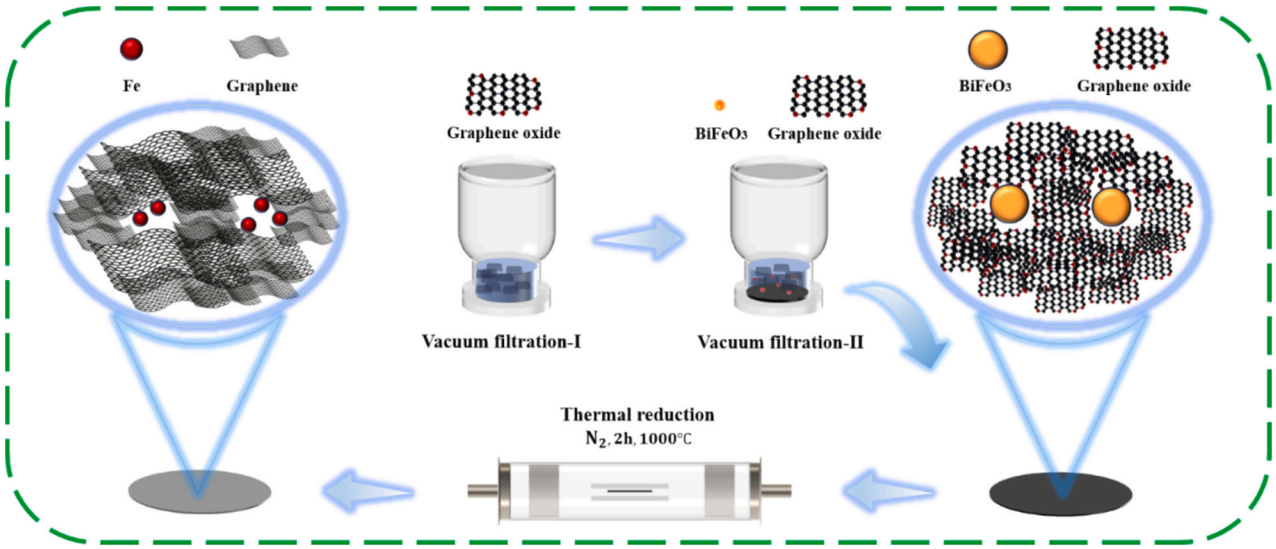


**Fig. 1.** Schematic of the FRGO film fabrication by two-step filtration and thermal annealing method.

conductivity at room temperature, in which the samples were cut in a circular shape with a radius of 20 mm. The magnetic properties of the composite films were measured using a vibrating sample magnetometer (VSM, 7404, LakeShore). The EMI shielding performance was evaluated in the wavelength range of 8.2–12.4 GHz by a dual-port vector network analyzer (VNA, MS46322B, Anritsu, Japan), using a waveguide with specific dimensions for the X-band. For testing, the film was cut in a circle shape with a radius of 20 mm, then clamped between the waveguides. Prior to EMI measurement, the VNA was calibrated using the transmission-reflection line method. The calculation of scattering parameters was presented in Supporting Information.

## 3. Results and discussions

A two-step preparation, *i.e.*, filtration and drying of GO followed by filtration of $BiFeO_3$-GO, was utilized to obtain the composite films, as shown in Fig. 1. Initially, iron particles instead of $BiFeO_3$ were used but the GO/Fe-GO films obtained were prone to break after drying, as shown in Figure S1a. This was attributed to the agglomeration of iron particles in the rGO/Fe-rGO film after annealing, as shown in Figure S1b. When $BiFeO_3$ was used, the decomposition of $BiFeO_3$ into iron nanoparticles and the reduction of GO were simultaneously achieved during the annealing at 1000 °C in a nitrogen atmosphere, resulting in the intercalation of iron nanoparticles into graphene films. For bare GO, FGO-2:40, FGO-6:40, and FGO-10:40, intact films were obtained with further annealing treatment. Figs. S1c and S1d show the optical images of rGO and FRGO-6:40 films, both of which exhibit a silvery metallic luster. However, for the $BiFeO_3$ mass of 15 or 20 mg, the GO films above and below $BiFeO_3$ layer are readily delaminated (Figs. S1e and S1f), as the binding between the upper and lower GO films is greatly reduced due to the existence of excessive $BiFeO_3$.

Figure S1g shows the typical surface morphology of the GO film made by vacuum filtration. Very differently, on the surface of FGO-6:40 film scattered $BiFeO_3$ particles are observed (Figure S1h). Fig. 2a shows the cross-sectional image of FGO-6:40 film, in which the lower and upper parts were obtained by the first and second filtration, respectively, as indicated by the red rectangles. The cross-sectional element mapping from energy dispersive spectrometer (EDS) for FGO-6:40 film demonstrates that the most $BiFeO_3$ particles are dispersed in the middle layer, and only a few are found in the upper layer (Fig. 2b). If the upper and lower parts of FGO-6:40 film are gently separated, abundant $BiFeO_3$ particles can be observed on the inner GO surface, as shown in Figs. 2c and S2a. $BiFeO_3$ particles are typically smaller than 10 μm in diameter. The EDS element mapping shows that C, O, Fe and Bi are distributed on the inner surface of FGO-6:40 film, and Fe/Bi is only found in the $BiFeO_3$ particles (Figure S2). Notably, the $BiFeO_3$ particles on the outer surface of FGO-6:40 is quite sparse (Figure S1h), in contrast to the inner surface of FGO-6:40 (Fig. 2c). From the images we can speculate that most $BiFeO_3$ particles in $BiFeO_3$-GO mixture quickly sink to the bottom due to their high density during the second vacuum filtration process.

After being annealed at 1000 °C under a nitrogen atmosphere, FGO was transformed into FRGO. When the upper and lower layers of FRGO film were peeled, the $BiFeO_3$ particles vanished. Instead, there are holes observed in FRGO, as shown in Fig. 2d (the inner surface of FRGO-6:40).

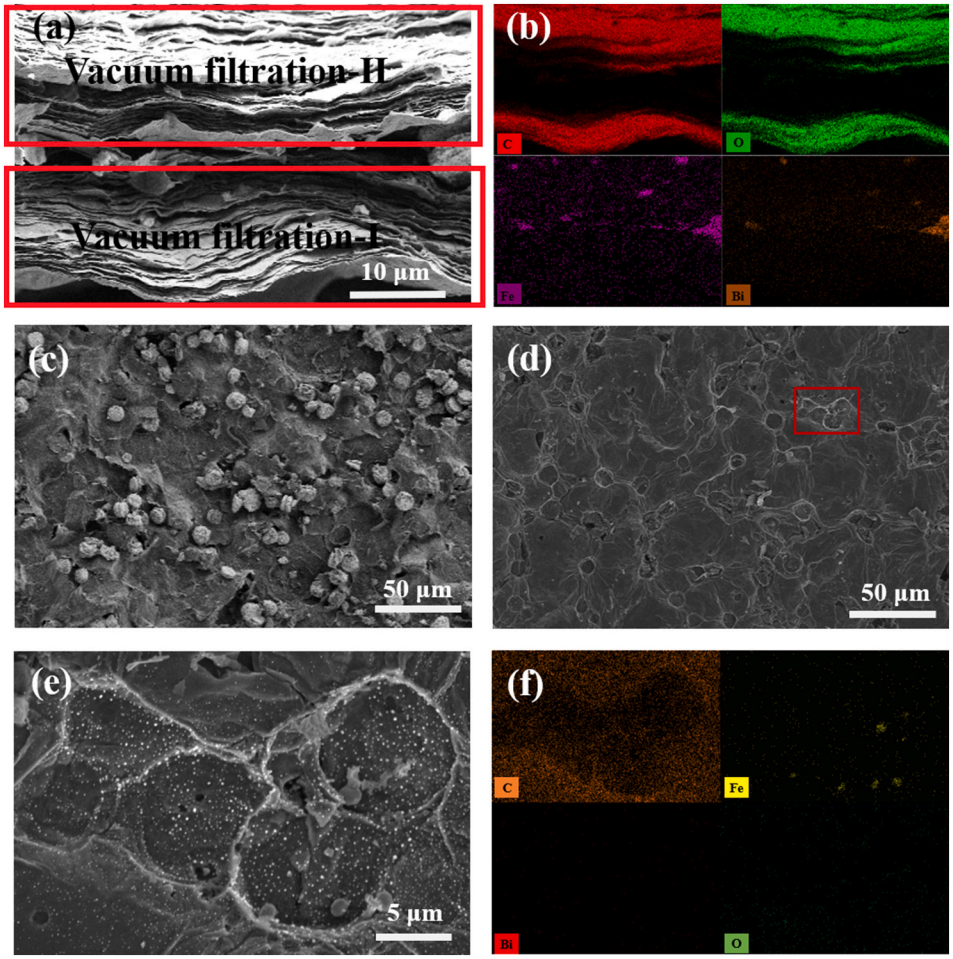


**Fig. 2.** (a) SEM image and (b) EDS element mapping of the cross section of FGO-6:40 film. The inner surface SEM images of (c) FGO-6:40 and (d-e) FRGO-6:40. (f) EDS element mapping of the area presented in (e).

The sizes of these holes (Fig. 2d) are close to those of the $BiFeO_3$ particles (Fig. 2c). Upon enlarging the selected area in Fig. 2d, fine particles scattered within the holes can be observed (Fig. 2e). The EDS element mapping of FRGO-6:40 in the area of Fig. 2e reveals that the main elements are C and Fe, while O and Bi are scarcely detected, as depicted in Fig. 2f. It has been reported that $BiFeO_3$ decomposes during high-temperature calcination due to the volatilization of bismuth ions. [28] Thermogravimetric analysis (TGA) of $BiFeO_3$ particles also indicates that as the temperature rises to 800 °C, the mass of the $BiFeO_3$ particles gradually decreases (Figure S3). When the temperature surpasses 800 °C, the $BiFeO_3$ particles themselves start to decompose, and a significant portion of Bi and O evaporates, leading to a sharp decline in mass (Figure S3). During the annealing at 1000 °C in our experiment, $BiFeO_3$ particles decomposed, and the spaces originally occupied by them turned into holes. XRD pattern reveals that the fine particles dispersed within these holes are iron particles (Fig. 3d). From TEM image, we can see that these iron particles are on the nanometer scale (Fig. 3a), with an average diameter of approximately 33.8 nm from a statistical analysis of 200 Fe particles (Fig. 3b), in great contrast to other Fe source like iron oxide (Figure S4). During the annealing at 1000 °C, the decomposition of $BiFeO_3$ particles and the reduction of GO both generate gas, [22,28] which causes the expansion of graphene layers in FRGO samples as shown in Figure S5. The thicknesses of rGO, FRGO-2:40, FRGO-6:40 or FRGO-10:40 (all with the similar areal loading of graphene) were measured as 38, 43, 71 or 95 μm, respectively.

Fig. 3c presents the Raman spectra obtained from the inner surfaces of FRGO-2:40, FRGO-6:40, FRGO-10:40, and rGO films. Two peaks located at 1334 and 1590 $cm^{-1}$ are attributed to D and G bands of rGO. [29] Through comparing the intensity ratio of these peaks, the intensity ratio ($I_D/I_G$) can be calculated as 1.22, 1.14, 1.16, and 1.22 for FRGO-2:40, FRGO-6:40, FRGO-10:40, and rGO films, respectively. The close $I_D/I_G$ values imply that the incorporation of $BiFeO_3$ particles into GO did not notably influence the reduction of GO during annealing process. Figure S6a presents the SEM image of the synthesized $BiFeO_3$ particles. It reveals that the size and morphology of these $BiFeO_3$ particles are essentially identical to those of the $BiFeO_3$ particles within FGO-6:40 (Fig. 2c and Figure S2a). Figure S6b depicts the XRD pattern from which distinct diffraction peaks at 22.5°, 31.8°, 32.1°, 39.0°, 39.5°, 45.8°, 51.3°, 51.8°, 56.4°, and 56.9° correspond to (101), (012), (110), (003), (021), (202), (113), (211), (104), and (122) planes of the $BiFeO_3$ crystal, respectively, as per the International Centre for Diffraction Data (ICDD) card #14–0181. From XRD patterns of rGO, FRGO-2:40, FRGO-6:40, and FRGO-10:40 illustrated in Fig. 3d, however, the characteristic peaks of $BiFeO_3$ vanish. Instead, diffraction peaks emerge at 25° and 44.5°, attributed to the (002) plane of graphene and the (110) plane of elemental iron, respectively. From FRGO-2:40 to FRGO-10:40, an increase in the intensity of iron signal is detected (Fig. 3d), indicating that the iron content in FRGO rises proportionally with the increase in the $BiFeO_3$ content within FGO. Additionally, a weak XRD signal of elemental bismuth can be discerned in FRGO-10:40, which implies that a certain amount of bismuth persists in the sample subsequent to the decomposition of $BiFeO_3$ at 1000 °C. The VSM results in Fig. 3e show that the saturation magnetic momentum of FRGO-2:40, FRGO-6:40 or FRGO-10:40 is 5.36, 23.66 and 35.04 emu/g, respectively, showing a gradual increase with more $BiFeO_3$ added. In contrast, the rGO film has a negligible magnetic momentum of 0.02 emu/g, demonstrating the magnetic contribution from iron nanoparticles as decomposed from $BiFeO_3$. According to the calculation of electromagnetic shielding formula, the enhancement of the electrical and magnetic properties of the material would lead to the increase of $SE_A$, thus the better shielding performance.

$$SE_A = 8.7d\sqrt{\pi f \mu \sigma}$$

where $d$ represents the effective thickness of the material, $f$ denotes the frequency of the incident electromagnetic wave, $\mu$ stands for the magnetic permeability, and $\sigma$ represents the electrical conductivity.

The electrical conductivity exerts a significant influence on the electromagnetic shielding performance. Fig. 4a depicts the electrical conductivities of rGO, FRGO-2:40, FRGO-6:40 or FRGO-10:40 films, which are 1150, 1220, 630 or 500 S $m^{-1}$, respectively. The slightly higher electrical conductivity of FRGO-2:40 than rGO is likely attributed to the incorporation of certain iron nanoparticles. For FRGO-2:40,

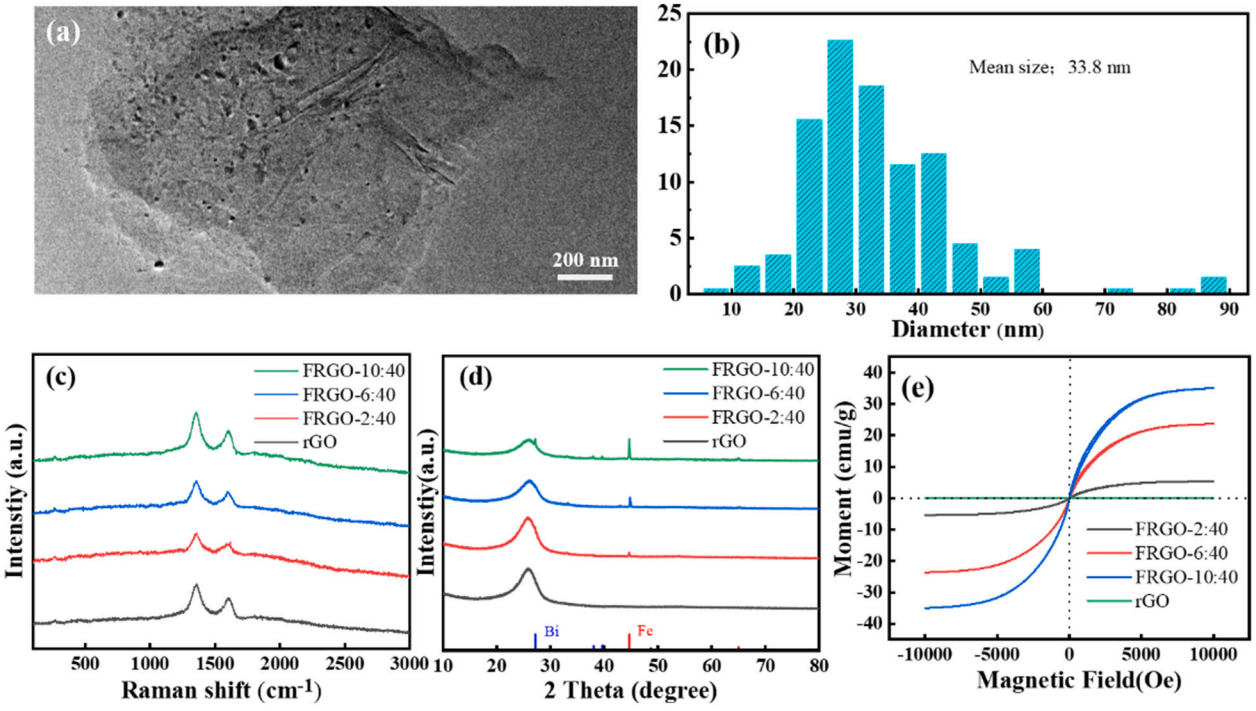


**Fig. 3.** (a) TEM image of FRGO-6:40. (b) Size distribution of iron nanoparticles within FRGO-6:40. (c) Raman spectra and (d) XRD patterns obtained from the inner surfaces of FRGO-2:40, FRGO-6:40, FRGO-10:40 and rGO films. (e) Magnetic hysteresis of FRGO-2:40, FRGO-6:40, FRGO-10:40, and rGO films.

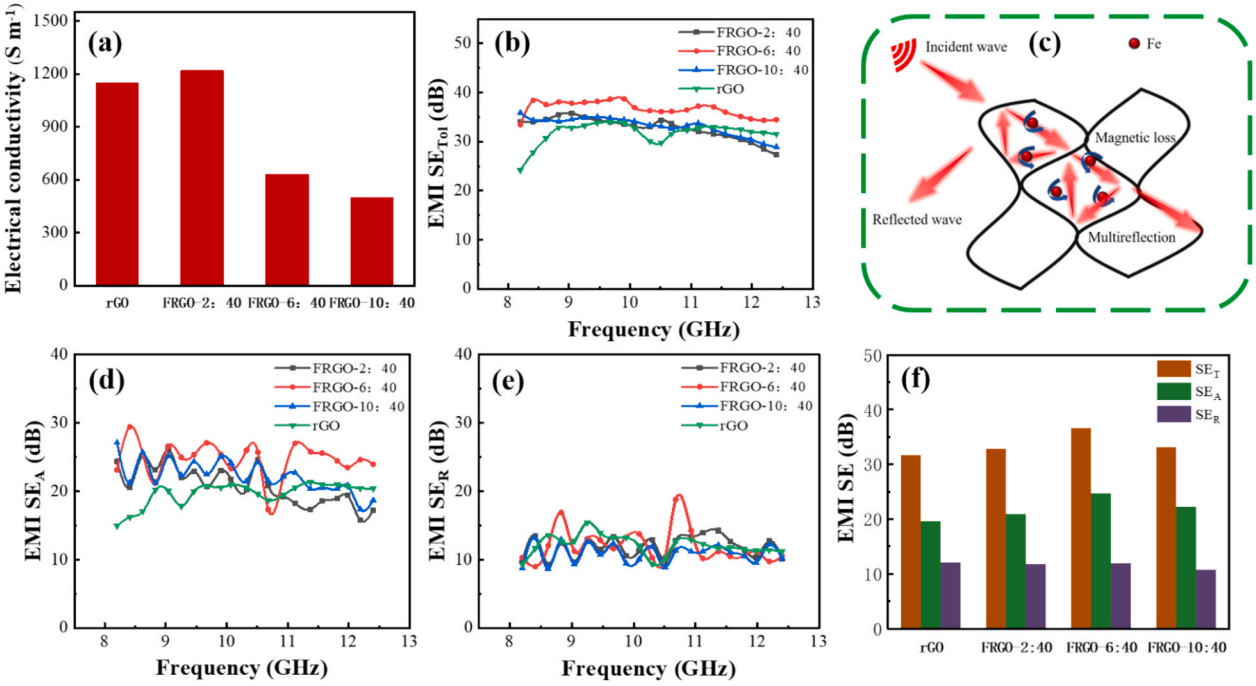


**Fig. 4.** (a) Electrical conductivity, (b) Shielding effectiveness of total ($SE_T$), (d) Shielding effectiveness of absorption ($SE_A$), and (e) Shielding effectiveness of reflection ($SE_R$) of FRGO-2:40 , FRGO-6:40 , FRGO-10:40, and rGO films. (c) Schematic illustration of electromagnetic wave absorption mechanisms in FRGO film. (f) Comparison of the contributions of $SE_T$, $SE_R$, and $SE_A$ among different samples.

FRGO-6:40 and FRGO-10:40, the electrical conductivities decline notably with the increase in the amount of $BiFeO_3$. This is probably due to the formation of more microholes and delamination in the interlayers of the FRGO films with an increasing amount of $BiFeO_3$ particles. These microholes and delamination would disrupt the electron transport channels within the graphene structure. Fig. 4b presents the total ($SE_T$) shielding effectiveness of each sample within X-band, calculated according to the formula provided in Supporting Information. The averaged $SE_T$ values of rGO, FRGO-2:40, FRGO-6:40 or FRGO-10:40 films are 31.72, 33.16, 36.63 or 32.83 dB, respectively. Among them, the FRGO-6:40 film demonstrates the optimal electromagnetic shielding performance, with $SE_T$ reaching 38.64 dB at 9.9 GHz. This performance is superior to that of the reported graphene/$Fe_3O_4$ film [30] and some other graphene-based composites (Table S1). [31–35] Figure S7 shows the absorptivity (A), reflectivity (R) and transmissivity (T) of rGO, FRGO-2:40, FRGO-6:40 and FRGO-10:40. The T value of the graphene-based composites ranges from $5.21 \times 10^{-4}$ to $2.17 \times 10^{-4}$, indicating that FRGO shields more than 99.9 % of the incident wave. It can be seen that the R value of all samples is much higher than A, suggesting a reflection dominated mechanism in EMI SE of FRGO. [36]

The EMI performance is closely associated with the electrical conductivity. Specifically, a decrease in the electrical conductivity leads to a reduction in $SE_T$. Nevertheless, compared to the rGO film, the electrical conductivity of FRGO-6:40 film decreases by 45.2 %, but the $SE_T$ increases by 15.5 %. This observation can be attributed to the microholes and iron nanoparticles that are intercalated within the inner layer of the FRGO-6:40 film. As schematically illustrated in Fig. 4c, the microholes can enhance the reflection of electromagnetic waves within the films, which would consequently lead to an increase in the absorption loss of electromagnetic waves. [14,37–39] Additionally, the iron nanoparticles, owing to their magnetic properties, are also capable of absorbing electromagnetic waves. [40,41] However, when comparing the $SE_T$ of FRGO-6:40 with that of FRGO-10:40, the further reduction in electrical conductivity in FRGO-10:40 has caused an overall decrease in $SE_T$.

We further evaluated the specific electromagnetic absorption ($SE_A$) and specific electromagnetic reflection ($SE_R$) to ascertain the primary contribution of iron nanoparticles and microholes to the EMI properties of FRGO films. The averaged $SE_A$ value of rGO, FRGO-2:40, FRGO-6:40 and FRGO-10:40 film is 19.62, 20.96, 24.67 or 22.33 dB (Fig. 4d), and the average $SE_R$ is 12.10, 11.87, 11.98 or 10.83 dB, respectively (Fig. 4e), as compared in Fig. 4f. It is evident that, in comparison with rGO film, the $SE_A$ values of FRGO films are increased, while their $SE_R$ remain largely unchanged. This indicates that iron nanoparticles and microholes indeed largely contribute to electromagnetic wave absorption.

## 4. Conclusions

In summary, $BiFeO_3$ was intercalated into the inner layer of GO film (FGO) *via* a two-step vacuum filtration method. When annealing the FGO at 1000 °C at nitrogen atmosphere, the $BiFeO_3$ decomposed, generating iron nanoparticles and microholes that were dispersed on the inner surface. Concurrently, the GO film was reduced to rGO film. By adjusting the ratio of $BiFeO_3$ to GO, FRGO with different contents of iron nanoparticles were obtained. Specifically, the $SE_T$ of the FRGO-6:40 film with a thickness of 71 μm reaches 38.64 dB at 9.9 GHz, superior to the rGO film. It is believed that these microholes and iron nanoparticles act synergistically to enhance the electromagnetic shielding performance of FRGO films.

## CRediT authorship contribution statement

**Xingnian Li:** Writing – original draft, Software, Methodology, Data curation. **Fei Wang:** Methodology, Data curation. **Qiang Li:** Writing – review & editing, Writing – original draft, Supervision, Data curation, Conceptualization. **Chuanren Ye:** Writing – review & editing, Supervision, Funding acquisition. **Yingyu Chen:** Software, Methodology. **Jingwei Li:** Software, Methodology. **Hui Lin:** Software, Data curation. **Jingwei Zhang:** Software, Methodology. **Yanwu Zhu:** Supervision, Funding acquisition, Data curation.

## Declaration of competing interest

The authors declare that they have no known competing financial interests or personal relationships that could have appeared to influence the work reported in this paper.

## Acknowledgements

The authors appreciate financial support provided by Hunan 208 Advanced Technology Company Limited (W2023JSFW0220), Innovation and Entrepreneurship Training Program for College Students in Hefei University of Technology (S202410359299) and Open Cooperation Foundation of the Department of Chemical Science of Henan University (DCSHENU2407). The authors also thank Dr. Bao Chao from the Institute of Solid State Physics, Hefei Institute of Physical Sciences, Chinese Academy of Sciences for the assistance of EMI SE test.

## Appendix A. Supplementary data

Supplementary data to this article can be found online at https://doi.org/10.1016/j.diamond.2025.112247.

## Data availability

Data will be made available on request.

## References

[1] S. Engels, N.-L. Schneider, N. Lefeldt, C.M. Hein, M. Zapka, A. Michalik, D. Elbers, A. Kittel, P.J. Hore, H. Mouritsen, Anthropogenic electromagnetic noise disrupts magnetic compass orientation in a migratory bird, Nature 509 (2014) 353–356.
[2] M. Zhang, X.X. Wang, W.Q. Cao, J. Yuan, M.S. Cao, Electromagnetic functions of patterned 2D materials for micro–nano devices covering GHz, THz, and optical frequency, Advanced Optical Materials 7 (2019) 1900689.
[3] Y. Zhang, Y. Huang, T. Zhang, H. Chang, P. Xiao, H. Chen, Z. Huang, Y. Chen, Broadband and tunable high-performance microwave absorption of an ultralight and highly compressible graphene foam, Adv. Mater. 27 (2015) 2049–2053.
[4] C. Wang, V. Murugadoss, J. Kong, Z. He, X. Mai, Q. Shao, Y. Chen, L. Guo, C. Liu, S. Angaiah, Z. Guo, Overview of carbon nanostructures and nanocomposites for electromagnetic wave shielding, Carbon 140 (2018) 696–733.
[5] F.M. Oliveira, L. Martins, N.V. Dencheva, T.A. Ezquerra, Z.Z. Denchev, Tunable electromagnetic interference shielding properties of binary thermoplastic composites prepared by reactive microencapsulation, ACS Applied Polymer Materials 4 (2022) 3482–3490.
[6] Y. Han, J. Yuan, Y. Zhu, Q. Wang, L. Li, M. Cao, Implantation of WSe2 nanosheets into multi-walled carbon nanotubes for enhanced microwave absorption, J. Colloid Interface Sci. 609 (2022) 746–754.
[7] Y. Wang, X. Jing, Intrinsically conducting polymers for electromagnetic interference shielding, Polym. Adv. Technol. 16 (2005) 344–351.
[8] D.D.L. Chung, Electromagnetic interference shielding effectiveness of carbon materials, Carbon 39 (2001) 279–285.
[9] M. Han, Y. Gogotsi, Perspectives for electromagnetic radiation protection with MXenes, Carbon 204 (2023) 17–25.
[10] H. Deng, T. Skipa, E. Bilotti, R. Zhang, D. Lellinger, L. Mezzo, Q. Fu, I. Alig, T. Peijs, Preparation of high-performance conductive polymer fibers through morphological control of networks formed by Nanofillers, Adv. Funct. Mater. 20 (2010) 1424–1432.
[11] Q. Wei, S. Pei, X. Qian, H. Liu, Z. Liu, W. Zhang, T. Zhou, Z. Zhang, X. Zhang, H. M. Cheng, W. Ren, Superhigh electromagnetic interference shielding of ultrathin aligned pristine graphene nanosheets film, Adv. Mater. 32 (2020) 1907411.
[12] X. Chen, D. Lai, Facile construction of flexible multilayered graphene-based composite films for excellent electromagnetic interference shielding with ultralow-reflection, Carbon 214 (2023) 118375.
[13] T. Xia, J. Cao, M.A. Bissett, H. Waring, Y. Xiang, G. Pinter, A.V. Kretinin, P. Yang, Y. Zhu, X. Zhao, S.A. Hodge, T. Thomson, I.A. Kinloch, Graphenization of graphene oxide films for strongly anisotropic thermal conduction and high electromagnetic interference shielding, Carbon 215 (2023) 118496.
[14] J. Xi, Y. Li, E. Zhou, Y. Liu, W. Gao, Y. Guo, J. Ying, Z. Chen, G. Chen, C. Gao, Graphene aerogel films with expansion enhancement effect of high-performance electromagnetic interference shielding, Carbon 135 (2018) 44–51.
[15] Z. Wang, G. Cai, Y. Xia, P. Li, S. Shi, B. Wang, W. Gao, Y. Liu, Z. Xu, C. Gao, Highly conductive graphene fiber textile for electromagnetic interference shielding, Carbon 222 (2024) 118996.
[16] M.S. Cao, X.X. Wang, M. Zhang, J.C. Shu, W.Q. Cao, H.J. Yang, X.Y. Fang, J. Yuan, Electromagnetic response and energy conversion for functions and devices in low-dimensional materials, Adv. Funct. Mater. 29 (2019) 1807398.
[17] K. Hantanasirisakul, Y. Gogotsi, Electronic and optical properties of 2D transition metal carbides and nitrides (MXenes), Adv. Mater. 30 (2018) e1804779.
[18] Y. Xia, W. Gao, C. Gao, A review on graphene-based electromagnetic functional materials: electromagnetic wave shielding and absorption, Adv. Funct. Mater. 32 (2022) 2204591.
[19] X. Yan, T. Ji, W. Ye, B.P. Singh, Surface modification of activated carbon fibers with Fe3O4 for enhancing their electromagnetic wave absorption property, J. Nanomater. 2020 (2020) 1–14.
[20] B.K.M. Van-Tam Nguyen, Yoonsik Yi, Seong Jun Kim, Choon-Gi Choi, MXene (Ti3C2TX)/graphene/PDMS composites for multifunctional broadband electromagnetic interference shielding skins, Chem. Eng. J. 393 (2020) 124608.
[21] B. Qiu, X. Zhang, S. Xia, T. Sun, Y. Ling, S. Zhou, H. Guang, Y. Chen, Z. Xu, M. Liang, H. Zou, Magnetic graphene oxide/carbon fiber composites with improved interfacial properties and electromagnetic interference shielding performance, Compos. A: Appl. Sci. Manuf. 155 (2022) 106811.
[22] C. Liang, Z. Gu, Y. Zhang, Z. Ma, H. Qiu, J. Gu, Structural design strategies of polymer matrix composites for electromagnetic interference shielding: a review, Nanomicro Lett 13 (2021) 181.
[23] X. Tang, J. Luo, Z. Hu, S. Lu, X. Liu, S. Li, X. Zhao, Z. Zhang, Q. Lan, P. Ma, Z. Wang, T. Liu, Ultrathin, flexible, and oxidation-resistant MXene/graphene porous films for efficient electromagnetic interference shielding, Nano Res. 16 (2022) 1755–1763.
[24] Y. Li, J. Cao, G. Chen, L. He, X. Du, J. Xie, Y. Wang, W. Hu, Scalable production of highly conductive 2D NbSe2 monolayers with superior electromagnetic interference shielding performance, ACS Appl. Mater. Interfaces 16 (2024) 6250–6260.
[25] H. Kashani, M. Giroux, I. Johnson, J. Han, C. Wang, M. Chen, Unprecedented electromagnetic interference shielding from three-dimensional bi-continuous Nanoporous graphene, Matter 1 (2019) 1077–1087.
[26] J. Yin, J. Zhang, S. Zhang, C. Liu, X. Yu, L. Chen, Y. Song, S. Han, M. Xi, C. Zhang, N. Li, Z. Wang, Flexible 3D porous graphene film decorated with nickel nanoparticles for absorption-dominated electromagnetic interference shielding, Chem. Eng. J. 421 (2021) 129763.
[27] H. Lv, G. Ji, X. Liang, H. Zhang, Y. Du, A novel rod-like MnO2@Fe loading on graphene giving excellent electromagnetic absorption properties, Journal of Materials Chemistry C 3 (2015) 5056–5064.
[28] L. Wu, W. Sui, C. Dong, C. Zhang, C. Jiang, One-dimensional BiFeO3 nanotubes: preparation, characterization, improved magnetic behaviors, and prospects, Appl. Surf. Sci. 384 (2016) 368–375.
[29] L.M. Malard, M.A. Pimenta, G. Dresselhaus, M.S. Dresselhaus, Raman spectroscopy in graphene, Phys. Rep. 473 (2009) 51–87.
[30] Z. Wang, B. Jiao, Y. Qing, H. Nan, L. Huang, W. Wei, Y. Peng, F. Yuan, H. Dong, X. Hou, Z. Wu, Flexible and transparent Ferroferric oxide-modified silver nanowire film for efficient electromagnetic interference shielding, ACS Appl. Mater. Interfaces 12 (2019) 2826–2834.
[31] W.-L. Song, X.-T. Guan, L.-Z. Fan, W.-Q. Cao, C.-Y. Wang, Q.-L. Zhao, M.-S. Cao, Magnetic and conductive graphene papers toward thin layers of effective electromagnetic shielding, J. Mater. Chem. A 3 (2015) 2097–2107.
[32] K. Singh, A. Ohlan, V.H. Pham, B. R., S. Varshney, J. Jang, S.H. Hur, W.M. Choi, M. Kumar, S.K. Dhawan, B.-S. Kong, J.S. Chung, Nanostructured graphene/Fe3O4 incorporated polyaniline as a high performance shield against electromagnetic pollution, Nanoscale 5 (2013) 2411–2420.
[33] M. Mishra, A.P. Singh, B.P. Singh, V.N. Singh, S.K. Dhawan, Conducting ferrofluid: a high-performance microwave shielding material, J. Mater. Chem. A 2 (2014) 13159–13168.
[34] H.-B. Zhang, Q. Yan, W.-G. Zheng, Z. He, Z.-Z. Yu, Tough graphene−polymer microcellular foams for electromagnetic interference shielding, ACS Appl. Mater. Interfaces 3 (2011) 918–924.
[35] Z. Chen, C. Xu, C. Ma, W. Ren, H.M. Cheng, Lightweight and flexible graphene foam composites for high-performance electromagnetic interference shielding, Adv. Mater. 25 (2013) 1296–1300.
[36] M. Peng, F. Qin, Clarification of basic concepts for electromagnetic interference shielding effectiveness, J. Appl. Phys. 130 (2021) 225108.
[37] Y. Zhang, Y. Huang, T. Zhang, H. Chang, P. Xiao, H. Chen, Z. Huang, Y. Chen, Broadband and tunable high-performance microwave absorption of an ultralight and highly compressible graphene foam, Adv. Mater. 27 (2015) 2049–2053.
[38] F. Xu, R. Chen, Z. Lin, X. Sun, S. Wang, W. Yin, Q. Peng, Y. Li, X. He, Variable densification of reduced graphene oxide foam into multifunctional high-performance graphene paper, J. Mater. Chem. C 6 (2018) 12321–12328.
[39] V. Shukla, Review of electromagnetic interference shielding materials fabricated by iron ingredients, Nanoscale Adv 1 (2019) 1640–1671.
[40] Z. Yu, Z. Yao, N. Zhang, Z. Wang, C. Li, X. Han, X. Wu, Z. Jiang, Electric field-induced synthesis of dendritic nanostructured α-Fe for electromagnetic absorption application, J. Mater. Chem. A 1 (2013) 4571–4576.
[41] G. Sun, B. Dong, M. Cao, B. Wei, C. Hu, Hierarchical dendrite-like magnetic materials of Fe3O4, γ-Fe2O3, and Fe with high performance of microwave absorption, Chem. Mater. 23 (2011) 1587–1593.